MODELLISTICA E CALCOLO SCIENTIFICO

MO X

MODELING AND SCIENTIFIC COMPUTING

MOX-Report No. 58/2017

Numerical approximation of the electromechanical coupling in the left ventricle with inclusion of the Purkinje network

Landajuela, M.; Vergara, C.; Gerbi, A.; Dede', L.; Formaggia, L.; Quarteroni, A.

Numerical approximation of the electromechanical coupling in the left ventricle with inclusion of the Purkinje network

Mikel Landajuela[1], Christian Vergara[1], Antonello Gerbi[2], Luca Dede'[1], Luca Formaggia[1] and Alfio Quarteroni[1,2]

November 2, 2017

[1] MOX– Modellistica e Calcolo Scientifico
Dipartimento di Matematica "F. Brioschi"
Politecnico di Milano
via Bonardi 9, 20133 Milano, Italy
email@mate.polimi.it

[2] Chair of Modelling and Scientific Computing
Institute of Mathematics
École Polytechnique Fédérale de Lausanne
CH-1015 Lausanne, Switzerland

Keywords: Computational electromechanics, Purkinje network, Pressure-Volume loop

Abstract

In this work, we consider the numerical approximation of the electromechanical coupling in the left ventricle with inclusion of the Purkinje network. The mathematical model couples the 3D elastodynamics and bidomain equations for the electrophysiology in the myocardium with the 1D monodomain equation in the Purkinje network. For the numerical solution of the coupled problem, we consider a fixed-point iterative algorithm that enables a partitioned solution of the myocardium and Purkinje network problems. Different levels of myocardium-network splitting are considered and analyzed. The results are compared with those obtained using standard strategies proposed in the literature to trigger the electrical activation. Finally, we present a physiological cardiac simulation, including the initiation of the signal in the Purkinje network, the systolic phase and the beginning of the filling phase.

1 Introduction

Computational modeling of the electromechanical coupling in the heart can be used to better understand the complex interplay between the chemical, electrical and mechanical fields that are involved in the cardiac cycle [1, 2, 3, 4, 5, 6, 7, 8, 9, 10, 11, 12, 13, 14, 15, 16, 17]. For instance, one may be interested in studying how a pathological condition of the electrical conduction system affects the overall contraction in the ventricles [18, 19]. The underlying motivation here is that outputs of computer-based simulations in patient-specific geometries can be used by the physicians to enhance diagnosis and therapy planning.

A key role in the propagation of the electric signal in the heart is played by the Purkinje fiber system. This is a complex network of cardiac cells located at the endocardium that is specialized in the rapid conduction of electric signals in the ventricles. In a normal cardiac cycle, the electric signal coming from the atrioventricular (AV) node travels along the Purkinje network and enters the myocardium through the Purkinje-muscle junctions (PMJ). After that, the signal is spread throughout the myocardium, thus triggering the reactions leading to the mechanical contraction [20].

So far, computational studies that include the Purkinje network have been mainly focused on its effects on the myocardium electrophysiology [21, 22, 23, 24, 25, 26, 27, 28, 29, 30, 31, 32, 33, 34], that is, without the consideration of the mechanical contraction. Works that study the role of the Purkinje network in the mechanical contraction of the heart are rare in the literature. On one hand, the fast conduction of the Purkinje network was included in [35] in a computational model of cardiac electromechanics through a surrogate spatial modification of the myocardial conduction properties. Therein, comparisons with experimental measurements showed the importance of the Purkinje fiber system in determining the mechanical activation sequence. On the other hand, a preliminary study of the effect of the Purkinje system in the electromechanical problem was also presented in [36], where a separate one-dimensional problem was solved for the propagation through the network. Still in [36], was observed that the network has an influence in the contraction, introducing an asymmetry in the ventricular depolarization.

Although these studies highlight the importance of including the Purkinje network when performing electromechanical simulations, a complete understanding of its effect in the mechanical contraction is still missing. In particular, the following aspects need to be addressed:

- a detailed study of the coupling strategy between the Purkinje and the myocardium solvers;

- a comprehensive comparison of the effect of the inclusion of the Purkinje network with respect to the standard surrogate models of activation found in the literature;

- a strategy to include the Purkinje network in simulations of the pressure-volume (PV) loop.

This paper aims at addressing all these points by integrating the electromechanical model developed in [37] (adapted to the bidomain model) with a model for the description of the electrophysiology in the Purkinje fibers network. It is organized as follows. In Section 2 we introduce the model that couples the equations modeling the signal propagation in the Purkinje network with the ones that describe the electromechanical contraction of the myocardium developed in [37]. In Section 3 we address the strategies for the numerical solution of such problems and present the coupling strategy adopted. Numerical experiments are presented in Section 4. In particular, a numerical comparison of two different coupling strategies is carried out in Section 4.2, whereas comparisons with standard surrogate models of the network are presented in Section 4.3. In Section 5, the strategy to embed the Purkinje electrophysiology in modeling the PV loop is described. Special attention is given there to the events happening in the Purkinje network throughout the cycle. Finally, a partial simulation of the PV loop, including the Purkinje fibers, is presented in Section 6.

2 Mathematical models

2.1 Electromechanical activation in the myocardium

The electrical and mechanical response of the heart largely depends on its highly anisotropic internal structure [14, 38]. As a matter of fact, the myocardium is composed of fibers wrapped in laminar collagen sheets. This structure is described, on a local frame of reference, by the vectorial fields $\mathbf{f}_0$ (fibers), $\mathbf{s}_0$ (sheets) and $\mathbf{n}_0$ (normals) defined over the myocardium. See Figure 1.

2.1.1 Myocardium electrophysiology.

In modeling the electrophysiology of the heart, we can distinguish between models for the cardiac cell electrophysiology, describing the bioelectric activity at the cell level independently of the rest of the cardiac function, and cardiac tissue models, accounting for the propagation of excitation throughout the cardiac muscle [10, 14, 26, 40, 41].

Cardiac cell electrophysiology models build upon the pioneering work of Hodgkin and Huxley [42]. They describe the transport of ionic species and the opening and closing dynamics of gating mechanisms throughout the cellular membrane. The general form of such models, written in the Hodgkin-Huxley

3
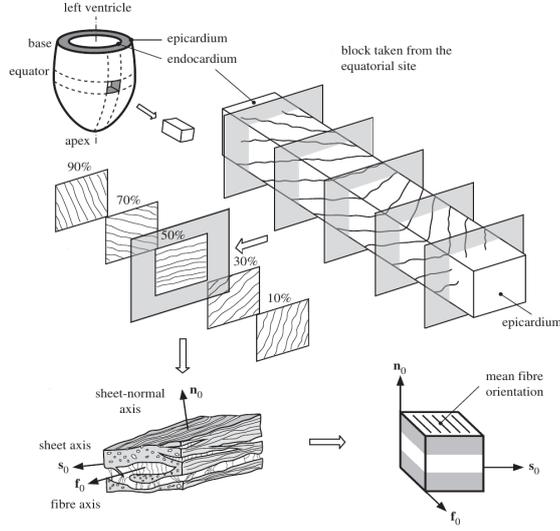
Figure 1: Structure of the cardiac myocardium. Image reproduced from [39].

formalism, consists in the following system of ODEs,

$$
\begin{aligned}
\frac{dv_m}{dt} + I_m^{ion}(v_m, \mathbf{w}_m) &= 0, \\
\frac{d\mathbf{w}_m}{dt} + f_m(v_m, \mathbf{w}_m) &= \mathbf{0},
\end{aligned}
\tag{1}
$$

where v_m is the transmembrane potential, $\mathbf{w}_m$ represents all concentration of ionic species and gating variables, the latter representing the percentage of open channels per unit area of the membrane; I_m^{ion} and f_m are, in general, non-linear terms driving the dynamics of the system. A wide range of models have been proposed in the last years, achieving different degrees of accuracy in their descriptions [43, 44, 45]. In this work, we consider the phenomenological Bueno-Orovio minimal model [46] as cellular model in the myocardium. This model is able to capture the main features of the action potential using only three variables , i.e., $\mathbf{w}_m = (w_1, w_2, w_3)$. The first two, w_1 and w_2, accounts for some gating processes whereas, the third one w_3 is strictly related to the calcium ionic concentration.

Model (1), describing the electrical activity at the microscopic level, can be incorporated into macroscopic descriptions at the tissue level. The cardiac cells are surrounded by extracellular species and connected by end-to-end and/or side-to-side junctions. A homogenization process of equation (1), taking into consideration the specific intra and extra cellular structure of the muscle tissue,

4

leads to the so called bidomain model (see [47, 48, 49, 50]), proposed in [51],

$$\chi_m \left(\mathcal{C}_m \frac{\partial v_m}{\partial t} + I_m^{ion}(v_m, \mathbf{w}_m) \right) - \nabla \cdot (\mathbf{D}_{i,m} \nabla v_m) - \nabla \cdot (\mathbf{D}_{i,m} \nabla u_{e,m}) = I^{ext},$$
$$-\nabla \cdot (\mathbf{D}_{e,m} \nabla v_m) - \nabla \cdot ((\mathbf{D}_{i,m} + \mathbf{D}_{e,m}) \nabla u_{e,m}) = 0, \tag{2}$$

where $u_{e,m}$ is the extracellular potential. Here, $\mathbf{D}_{i,m}$ and $\mathbf{D}_{e,m}$ are diffusion tensors defined as

$$\mathbf{D}_{i,m} = \sigma_{i,t}\mathbf{I} + (\sigma_{i,l} - \sigma_{i,t})\,\mathbf{f}_0 \otimes \mathbf{f}_0, \quad \mathbf{D}_{e,m} = \sigma_{e,t}\mathbf{I} + (\sigma_{e,l} - \sigma_{e,t})\,\mathbf{f}_0 \otimes \mathbf{f}_0,$$

where $\sigma_{i,t}, \sigma_{i,l}$ (respectively, $\sigma_{e,t}, \sigma_{e,l}$) are the conductivities in the orthogonal and longitudinal directions of the intracellular (respectively, extracellular) mediums with respect to the fibers direction $\mathbf{f}_0$. Parameters χ_m and $\mathcal{C}_m$ in (2) stand for the surface-to-volume ratio of the cell membrane and the membrane capacitance, respectively. The source term I^{ext} represents an external current for the myocardium which could be provided by the electrophysiology of the Purkinje fibers and/or by an applied current.

2.1.2 Myocardium mechanics.

We denote by $\mathbf{d}$ the myocardium displacement defined in the reference configuration of the myocardium $\Omega_0 \subset \mathbb{R}^3$. In this paper, subindex 0 always refers to fields or subdomains in the reference configuration. For the discussion of the elastic constitutive model, we classically introduce the gradient of deformation $\mathbf{F} = \boldsymbol{I} + \nabla_0 \mathbf{d}$, the Jacobian $J = \det(\mathbf{F})$ and the right Cauchy-Green strain tensor $\mathbf{C} \coloneqq \mathbf{F}^T \mathbf{F}$. Moreover, we consider the following invariants of $\mathbf{C}$,

$$\mathcal{I}_1 = \operatorname{tr} \mathbf{C}, \quad \mathcal{I}_{4,f} = \mathbf{C} : \mathbf{f}_0 \otimes \mathbf{f}_0 = \mathbf{f} \otimes \mathbf{f},$$
$$\mathcal{I}_{4,s} = \mathbf{C} : \mathbf{s}_0 \otimes \mathbf{s}_0 = \mathbf{s} \otimes \mathbf{s}, \quad \mathcal{I}_{8,fs} = \mathbf{C} : \mathbf{f}_0 \otimes \mathbf{s}_0 = \mathbf{f} \otimes \mathbf{s}.$$

Several constitutive models have been proposed in the literature to account for the orthotropic response of the heart muscle [52, 53, 39]. In this work, we consider the strain-energy function proposed by Holzapfel and Ogden in [39]. Also, we account for the nearly-incompressible nature of the myocardium by adding an extra convex term in J such that large volume variations are penalized (see [37] for the details). The final strain-energy function reads as follows:

$$\mathcal{W}(\mathbf{C}, J) = \frac{a}{2b}(e^{b(J^{-\frac{2}{3}}\mathcal{I}_1 - 3)} - 1) + \sum_{i=f,s} \frac{a_i}{2b_i}(e^{b_i(\mathcal{I}_{4,i}-1)^2} - 1) + \frac{a_{fs}}{2b_{fs}}(e^{b_{fs}(\mathcal{I}_{8,fs}^2 - 1)} - 1)$$
$$+ \frac{B}{2}(J + J\ln J - 1), \tag{3}$$

where the parameters B (bulk modulus) and $a, b, a_f, b_f, a_s, b_s, a_{fs}, b_{fs}$ are experimentally fitted. Model (3) is used to describe the passive response of the

heart myocardium. In order to account for the active response of the muscle, we follow the active-strain approach [38, 54, 55]. This entails a Lee-type multiplicative decomposition of $\mathbf{F}$ of the form $\mathbf{F} = \mathbf{F}_e\,\mathbf{F}_a(\gamma_f)$, where γ_f is an auxiliary dimensionless variable, which represents the local stretching (or elongation) of the fibers and whose dynamics are discussed below.

The non-linear elastodynamics equations read as

$$\rho\frac{\partial^2 \mathbf{d}}{\partial t^2} - \nabla_0 \cdot \mathbf{P}(\mathbf{d}, \gamma_f) = \mathbf{0} \tag{4}$$

where ρ is myocardium density and $\mathbf{P}$ is the second Piola-Kirchhoff stress tensor, that depends also on γ_f. We refer to [14] for a detailed description of the active-strain approach as well as for the final structure of the second Piola-Kirchhoff stress tensor.

2.1.3 Myocardium electromechanical coupled problem.

The active component $\mathbf{F}_a(\gamma_f)$ of the deformation tensor has not been defined yet. Following [37], the dynamics of γ_f, linking electrophysiology and mechanics, are modeled by a reaction-diffusion system of the form

$$\mu_A w_3^2 \frac{\partial \gamma_f}{\partial t} - \varepsilon\Delta\gamma_f = \Phi(w_3, \gamma_f, \mathbf{d}), \tag{5}$$

where μ_A is a physiological viscosity parameter and ε is a regularization parameter both to be properly tuned. The function $\Phi(w_3, \gamma_f, \mathbf{d})$ determines the activation dynamics depending on the concentration of calcium ions (here, assimilated to the variable w_3), and the displacement, so that the sarcomere force-length relationship is taken into account [56]. We refer to [37] for the specific structure of this function.

We impose the following orthotropic structure to the active deformation tensor

$$\mathbf{F}_a = \mathbf{I} + \gamma_f \mathbf{f}_0 \otimes \mathbf{f}_0 + \gamma_s \mathbf{s}_0 \otimes \mathbf{s}_0 + \gamma_n \mathbf{n}_0 \otimes \mathbf{n}_0,$$

with $\gamma_n = \gamma_n(\gamma_f), \gamma_s = \gamma_s(\gamma_f, \gamma_n)$, representing the local shortening (or elongation) in the normal and sheet directions, respectively. These functions have to be chosen to reproduce the non-homogeneous transversal thickening of the ventricle's wall, while maintaining $\det(\mathbf{F}_a) = 0$. More specifically, we consider

$$\gamma_n = f(\lambda)\left(\frac{1}{\sqrt{1+\gamma_f}} - 1\right),$$

where λ represents the transmural coordinate, ranging from λ_{endo} at the endocardium to λ_{epi} at the epicardium, with the following expression proposed in [57] and exploited in [37],

$$f(\lambda) = k_{endo}\frac{\lambda - \lambda_{epi}}{\lambda_{endo} - \lambda_{epi}} + k_{epi}\frac{\lambda - \lambda_{endo}}{\lambda_{epi} - \lambda_{endo}}, \tag{6}$$

where k_{endo} and k_{epi} are suitable constants. Finally, as in [57], we set

$$\gamma_s = \frac{1}{(1 + \gamma_f)(1 + \gamma_n)} - 1.$$

Thus, the electromechanical coupled problem in the myocardium reads:
Find v_m, $\mathbf{w}_m$, $u_{e,m}$, $\mathbf{d}$, γ_f such that

$$\chi_m \left(\mathcal{C}_m \frac{\partial v_m}{\partial t} + I_m^{ion}(v_m, \mathbf{w}_m) \right) - \nabla_0 \cdot (J\mathbf{F}^{-1}\mathbf{D}_{i,m}\mathbf{F}^{-T}\nabla_0 v_m)$$
$$-\nabla_0 \cdot (J\mathbf{F}^{-1}\mathbf{D}_{i,m}\mathbf{F}^{-T}\nabla_0 u_{e,m}) = I^{ext} \quad \text{in} \quad \Omega_0 \times (0, T), \tag{7a}$$

$$-\nabla_0 \cdot (J\mathbf{F}^{-1}\mathbf{D}_{e,m}\mathbf{F}^{-T}\nabla_0 v_m) - \nabla_0 \cdot (J\mathbf{F}^{-1}(\mathbf{D}_{i,m} + \mathbf{D}_{e,m})\mathbf{F}^{-T}\nabla_0 u_{e,m}) = 0 \quad \text{in} \quad \Omega_0 \times (0, T), \tag{7b}$$

$$\frac{\partial \mathbf{w}_m}{\partial t} + f_m(v_m, \mathbf{w}_m) = 0 \quad \text{in} \quad \Omega_0 \times (0, T), \tag{7c}$$

$$\rho \frac{\partial^2 \mathbf{d}}{\partial t^2} - \nabla_0 \cdot \mathbf{P}(\mathbf{d}, \gamma_f) = \mathbf{0} \quad \text{in} \quad \Omega_0 \times (0, T), \tag{7d}$$

$$\mu_A w_3^2 \frac{\partial \gamma_f}{\partial t} - \varepsilon \Delta_0 \gamma_f = \Phi(w_3, \gamma_f, \mathbf{d}) \quad \text{in} \quad \Omega_0 \times (0, T), \tag{7e}$$

together with the following boundary conditions

$$(J\mathbf{F}^{-1}\mathbf{D}_{i,m}\mathbf{F}^{-T}\nabla_0 v_m) \cdot \mathbf{N} + (J\mathbf{F}^{-1}\mathbf{D}_{i,m}\mathbf{F}^{-T}\nabla_0 u_{e,m}) \cdot \mathbf{N} = 0, \quad \text{on} \quad \partial\Omega_0 \times (0, T), \tag{8a}$$

$$(J\mathbf{F}^{-1}\mathbf{D}_{e,m}\mathbf{F}^{-T}\nabla_0 u_{e,m}) \cdot \mathbf{N} = 0, \quad \text{on} \quad \partial\Omega_0 \times (0, T), \tag{8b}$$

$$(\mathbf{N} \otimes \mathbf{N}) \left(K_\perp^j \mathbf{d} + C_\perp^j \frac{\partial \mathbf{d}}{\partial t} \right) + (\mathbf{I} - \mathbf{N} \otimes \mathbf{N}) \left(K_\parallel^j \mathbf{d} + C_\parallel^j \frac{\partial \mathbf{d}}{\partial t} \right)$$
$$+ \mathbf{P}(\mathbf{d})\mathbf{N} = \mathbf{0} \quad \text{on} \quad \Gamma_0^j \times (0, T), \tag{8c}$$

$$\mathbf{P}(\mathbf{d})\mathbf{N} = p_{endo}(t)\mathbf{N} \quad \text{on} \quad \Gamma_0^{endo} \times (0, T), \tag{8d}$$

$$\nabla_0 \gamma_f \cdot \mathbf{N} = 0 \quad \text{on} \quad \partial\Omega_0 \times (0, T), \tag{8e}$$

where $\mathbf{N}$ denotes the outward-directed unit normal vector of the myocardium boundaries. Equations (8a)-(8b) account, as usual, for the electric insulation of the cardiac tissue. Note that the extracellular potential $u_{e,m}$ is defined up to a time-dependent constant. In this work, we fix that constant by enforcing

the value of $u_{e,m}$ to be zero at a selected point. In (8c), Γ_0^j, $j \in \{epi, base\}$, is the part of the boundary corresponding to the epicardium and the base of the myocardium. See Figure 2. On these subsets of the boundaries, mixed Robin conditions are set to mimic the effect of the pericardial sac (see [37]). The parameters $K_\perp^j, K_\parallel^j, C_\perp^j, C_\parallel^j \in \mathbb{R}^+$ are set to effectively support the myocardium, allowing however the physiological ventricle torsion and deformation in the pericardial sac. In (8d), the pressure $p_{endo}(t)$ represents the load produced by the blood on the endocardium. In this work, since we are not simulating the blood flowing in the ventricle, $p_{endo}(t)$ is either a given function taken from the literature (see the results in Section 5) or will be provided by the solution of a Windkessel zero dimensional model representing the electromechanical-fluid problem (see Section 6). Note that $\partial\Omega_0 = \Gamma_0^{base} \cup \Gamma_0^{endo} \cup \Gamma_0^{epi}$.
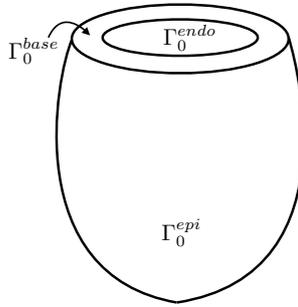
Figure 2: Computational domain of the myocardium.

Remark 1 *The bidomain model* (2) *is written in* (7) *in the reference configuration* Ω_0. *This entails the presence of the quantities* **F** *and* J *multiplying the diffusion tensors and, thus, the implicit dependence of* (2) *on the myocardium displacement* **d**.

In what follows, problem (7) is compactly written as follows

$$\boldsymbol{P}_m(v_m, u_{e,m}, \mathbf{w}_m, \mathbf{d}, \gamma_f, I^{ext}) = \mathbf{0}. \tag{9}$$

2.2 Electrical activation in the Purkinje network

In this paper, following [58], we assume that the Purkinje network domain lays in the reference configuration and is given by $\Omega_0^p = \bigcup_{i=1}^P S_{i,0}$, with $S_{i,0}$ denoting a straight segment. See Figure 3.

Due to the ventricle contraction, the Purkinje network deforms. In the following, we assume the current deformed network Ω^p is such that $\Omega^p = \bigcup_{i=1}^P S_i$, with $S_i = \phi_i(S_{i,0})$ and ϕ_i an affine transformation. We denote by $L_{i,0}$ and L_i the lengths of segments $S_{i,0}$ and S_i, respectively.

In order to model the potential propagation through the Purkinje network, we follow the approach proposed in [58], which is briefly discussed in this section. For further details, see also [32, 34].

The basic idea is to solve the 1D monodomain equation in each segment S_i, for $i \in \{1, \ldots, P\}$. The monodomain model emerges as a simplification of the bidomain model (2), when the hypothesis of equal anisotropy ratio in the intra and extracellular domains is made [10]. The 1D monodomain equation in each segment reads as follows:

$$\chi_p \left(\mathcal{C}_p \frac{\partial v_p}{\partial t} + I_p^{ion}(v_p, \mathbf{w}_p) \right) - \frac{\partial}{\partial l} \left(\sigma_p \frac{\partial v_p}{\partial l} \right) = 0, \tag{10}$$

where v_p is the transmembrane potential and l denotes the spatial coordinate along the segment. Equation (10) has to be complemented with suitable equations for the dynamics of the ionic species and gating variables $\mathbf{w}_p$ of the form of $(1)_2$.
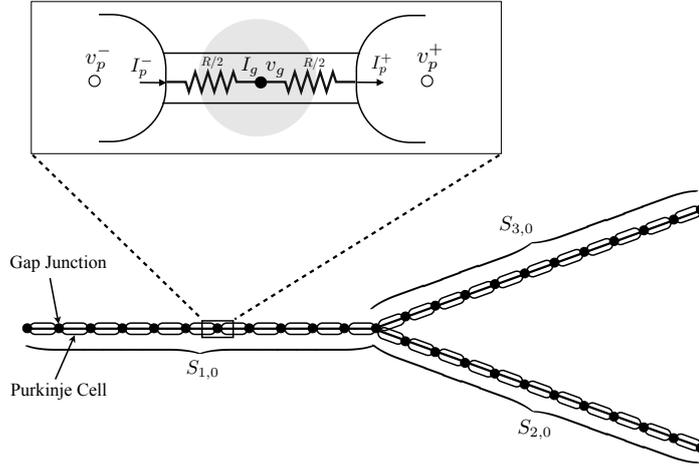
Figure 3: Schematic representation of a Purkinje network with three segments and one bifurcation.

The solutions are coupled through interface conditions over the branching nodes determined by the continuity of the potential and the Kirchhoff's current law. In order to set this law at each of the branching nodes, we opt to explicitly model the gap junctions between Purkinje cells, following [58]. For this purpose, we consider a sequence of units composed by two Purkinje cells connected by a gap junction. Each elementary unit lays in the same spatial coordinates. For each unit the unknowns of the problem are the transmembrane potentials v_g, v_p^+, v_p^- and the currents I_g, I_p^+, I_p^-. See the sketch in Figure 3. At the gap-junctions we have, according to Ohm's law,

$$I_g = \pm \frac{v_g - v_p^{\pm}}{R_g/2}. \tag{11}$$

9

Also, the intracellular current $I_p^{\pm}$ at the Purkinje cell can be written as

$$I_p^{\pm} = -\pi \varrho^2 \sigma_p \frac{\partial v_p^{\pm}}{\partial l},$$

where σ_p is the equivalent intracellular conductivity [58] and ϱ is the radius of the Purkinje cell. The Kirchhoff's current law at the gap-junction implies that

$$I_g = -\pi \varrho^2 \sigma_p \frac{\partial v_p^+}{\partial l} = \pi \varrho^2 \sigma_p \frac{\partial v_p^-}{\partial l}. \tag{12}$$

Finally, due once again to the Kirchhoff laws, the conditions at the branching nodes are

$$\sum_{j=1}^{q} I_{g,j} = 0, \qquad v_{g,1} = \cdots = v_{g,q}, \tag{13}$$

where q is the number of branches issuing from the bifurcation.

In the following, an extra subindex i in a variable will be used to specify that the corresponding variable lays in segment S_i, $i = 1, \ldots, P$. Considering the monodomain equation (10) written in each segment of the network for $v_{p,i}^{\pm}$ and $\mathbf{w}_{p,i}^{\pm}$, together with the gap-junctions relations (11)-(12) written in each segment of the network for $v_{g,i}^{\pm}$ and $I_{g,i}$, we arrive to the following problem: Find $v_{p,i}^{\pm}$, $\mathbf{w}_{p,i}^{\pm}$, $v_{g,i}$ and $I_{g,i}$, $i = 1, \ldots, P$, such that

$$\chi_p \left(\mathcal{C}_p \frac{\partial v_{p,i}^{\pm}}{\partial t} + I_p^{ion}(v_{p,i}^{\pm}, \mathbf{w}_{p,i}^{\pm}) \right)$$

$$- \left(\frac{L_{i,0}}{L_i(\mathbf{d})} \right) \frac{\partial}{\partial l} \left(\sigma_p \frac{\partial v_{p,i}^{\pm}}{\partial l} \right) = 0 \quad \text{in} \quad S_{i,0} \times (0,T], \quad i = 1, \ldots, P, \tag{14a}$$

$$\frac{\partial \mathbf{w}_{p,i}^{\pm}}{\partial t} + f_p(v_{p,i}^{\pm}, \mathbf{w}_{p,i}^{\pm}) = \mathbf{0} \quad \text{in} \quad S_{i,0} \times (0,T], \quad i = 1, \ldots, P, \tag{14b}$$

$$v_{g,i} = v_{p,i}^+ + \frac{I_{g,i} R_g}{2} = v_{p,i}^- - \frac{I_{g,i} R_g}{2} \quad \text{in} \quad S_{i,0} \times (0,T], \quad i = 1, \ldots, P, \tag{14c}$$

$$I_{g,i} = -\pi \varrho^2 \sigma_p \frac{\partial v_{p,i}^+}{\partial l} = \pi \varrho^2 \sigma_p \frac{\partial v_{p,i}^-}{\partial l} \quad \text{in} \quad S_{i,0} \times (0,T], \quad i = 1, \ldots, P, \tag{14d}$$

together with the following interface and boundary conditions,

$$\sum_{i=i_1^k}^{i_{q_k}^k} I_{g,i} = 0 \quad \text{at} \quad \boldsymbol{b}_k, \, k = 1, \ldots, P, \, t \in (0,T], \tag{15a}$$

$$v_{g,i_1^k} = \ldots = v_{g,i_{q_k}^k} \quad \text{at} \quad \boldsymbol{b}_k, \, k = 1, \ldots, P, \, t \in (0,T], \tag{15b}$$

$$-\pi \sigma_p \varrho^2 \frac{\partial v_p^{\pm}}{\partial l}(\boldsymbol{g}_{AV}) = h_{AV} \quad t \in (0,T], \tag{15c}$$

$$-\pi \sigma_p \varrho^2 \frac{\partial v_p^{\pm}}{\partial l}(\boldsymbol{g}_j) = h_j \quad j = 1, \ldots, N, \, t \in (0,T]. \tag{15d}$$

Here, $\boldsymbol{b}_k$, $k = 1, \ldots, P$, are the coordinates of the bifurcation and intersection points, $\boldsymbol{g}_{AV}$ represents the coordinates of the AV node, $\boldsymbol{g}_j$, $j = 1, \ldots, N$, the coordinates of the PMJ, and h_{AV} and h_j, $j = 1, \ldots, P$, prescribed currents. The indices $i_1^k, \ldots, i_{q_k}^k$ are the q_k indices related to the potentials and currents involved at the bifurcation/intersection point $\boldsymbol{b}_k$.

Remark 2 *The monodomain model* (10) *is written in* (14) *in the reference configurations $S_{i,0}$. This entails the presence of the ratio $\frac{L_{i,0}}{L_i(\mathbf{d})}$ multiplying the diffusion term and, thus, the implicit dependence of* (10) *on the myocardium displacement $\mathbf{d}$.*

Note that Neumann boundary conditions are imposed at the PMJ, via equation (15d). As a matter of fact, this is where the myocardium and network coupling takes place. The definition of the terms h_j is postponed until section 2.3.

In what follows, problem (14) is compactly written as follows

$$\boldsymbol{P}_p(v_p^+, v_p^-, v_g, I_g, \mathbf{w}_p^+, \mathbf{w}_p^-, \mathbf{d}, \mathbf{h}) = \mathbf{0},$$

where the unknowns are defined globally in all the network starting from their value on each segment $S_{i,0}$ and $\mathbf{h}$ is the vector collecting h_j for $j = 1, \ldots, N$.

2.3 Myocardium-Purkinje network coupled problem

The coupling between the myocardium and the network takes place at the PMJ. More specifically, the coupling is performed through the exchange of the currents φ_j, $j = 1, \ldots, N$, computed at the PMJ. From the myocardium perspective, PMJ currents φ_j are prescribed as external currents with support in spheres of radius r centered at the PMJ [59, 32]. From the network side, the PMJ currents φ_j are imposed as Neumann boundary conditions, see (15d). Moreover, following [59, 58], we model the junction as a resistance, so that, according to Ohm's law, the current φ_j at the jth PMJ can be written as follows

$$\varphi_j = \frac{\frac{v_p^+(\boldsymbol{g}_j) + v_p^-(\boldsymbol{g}_j)}{2} - \frac{1}{A_r} \int_{\mathcal{B}_r(\boldsymbol{g}_j)} v_m \, d\boldsymbol{x}}{R_{PMJ}}, \quad j = 1, \ldots, N, \ t \in (0, T], \quad (16)$$

where $\mathcal{B}_r(\boldsymbol{g}_j)$ is the sphere of radius r centered at the point $\boldsymbol{g}_j$, A_r the volume of this sphere and R_{PMJ} the resistance of the PMJ (supposed to be the same for all the PMJ).

Using the notation introduced in the previous sections, the coupled electromechanical/network problem reads: For each t, find $v_p^+, v_p^-, v_g, I_g, \mathbf{w}_p^+, \mathbf{w}_p^-, v_m, u_{e,m}, \mathbf{w}_m, \mathbf{d}, \gamma_f,$ and φ_j, $j = 1, \ldots, N$, such that

$$\begin{aligned}
\boldsymbol{P}_m\left(v_m, u_{e,m}, \mathbf{w}_m, \mathbf{d}, \gamma_f, \sum_{j=1}^N \frac{1}{A_r} \mathcal{I}_{\mathcal{B}_r(\boldsymbol{s}_j)} \varphi_j\right) &= \mathbf{0}, \\
\boldsymbol{P}_p\left(v_p^+, v_p^-, v_g, I_g, \mathbf{w}_p^+, \mathbf{w}_p^-, \mathbf{d}, \boldsymbol{\varphi}\right) &= \mathbf{0}, \\
\boldsymbol{P}_{PMJ}\left(v_p^+, v_p^-, v_m, \boldsymbol{\varphi}\right) &= \mathbf{0},
\end{aligned} \quad (17)$$

where the last equation in (17) represents the relations (16), $\mathcal{I}_Y$ is the characteristic function related to the region $Y \subset \Omega_m$, and $\boldsymbol{\varphi}$ is the vector collecting φ_j for $j = 1, \ldots, N$. In this case the external current is provided by the interaction with the PMJ.

3 Numerical solution

3.1 Fixed-point strategy for the coupled problem

In order to solve the coupled problem (17), we follow the framework proposed in [32] for the electrophysiology problem. The idea is to solve the coupled problem in a staggered way by iterating between the myocardium and the Purkinje network problems. The variables linking the two subproblems are the currents $\boldsymbol{\varphi}$ at the PMJ given by (16).

In the following, given a function z, we denote by z^n the approximation of z at time $t^n = n\Delta t$, where Δt is the time step. The discretization in time of the electromechanical problem (7) is carried out through an implicit scheme, as described in [37], involving second order Backward Differentiation Formulae for the approximation of the first and second time derivatives. Note that this involves a highly non-linear system at each time-step which is solved using the Newton method. A brief description of the resulting problem is presented in the Section 3.2 (see [37] for a detailed description).

The time discretization of the Purkinje network problem (14) is performed via a semi-implicit scheme, based on the operator splitting approach introduced in [58]. Basically, the time marching of the problem is split into four sequential stages (see [58, 32, 34]), with the reaction and diffusion terms being solved in different steps. The reaction term and the ionic model are solved in an explicit way, whereas the diffusion term is solved implicitly. The space discretization of the resulting diffusion equation is briefly discussed in Section 3.3 (see [58, 32] for further details).

The algorithm we propose for the numerical solution of the time discretization of the coupled problem (17) is presented in Algorithm 1. In the numerical experiments carried out in this work, we will explore the possibility of reducing the computational cost by considering a loosely coupled approach, that is taking $K_{max} = 1$ in Algorithm 1. The results will be compared with a fully implicit approach, in which Algorithm 1 is run until converge ($K_{max} = \infty$). In what follows, we provide a brief description of the space discretization of subproblems (19)-(20) in Algorithm 1.

Remark 3 *Note that we are using different time schemes for the myocardium and the Purkinje network problems. As a matter of fact, the former is solved with an implicit scheme, whereas for the latter we use a semi-implicit scheme. We are aware that this could lead to instabilities within the fixed-point strategy, but we did not find them in our numerical experiments. Furthermore, this shows*

in passing the intrinsic modularity of our coupling strategy: different solvers, with different time-discretizations, may be used for the two subproblems.

3.2 Space discretization of the electromechanical problem in the myocardium

For the numerical solution of problem (19) we follow the monolithic solution framework proposed in [37]. The space discretization is based on the Finite Elements method. Special treatment is given to the ionic currents, i.e., the term I_m^{ion} in (7a). More precisely, in order to integrate that term in the resulting weak form we consider the State Variable Interpolation (SVI) approach, i.e., we consider the unknown fields v_m and $\mathbf{w}_m$ interpolated at the quadrature nodes and then evaluate the function $I_m^{ion}(v_m, \mathbf{w}_m)$ at these arguments (see [60, 37]).

In the following, we will use capital letters in bold to denote vectors containing the approximations of fields at the degrees of freedom coming from the Finite Element discretization. At time step $n+1$, the linear system arising at the Newton iteration $k+1$ reads as follows (the current temporal index $n+1$ being understood):

$$\begin{pmatrix} \mathcal{A}_{\mathbf{W}} & \mathcal{A}_{\mathbf{WV}} & 0 & 0 & 0 \\ \mathcal{A}_{\mathbf{VW}} & \mathcal{A}_{\mathbf{V}} & \mathcal{A}_{\mathbf{VU}_e} & 0 & \mathcal{A}_{\mathbf{VD}} \\ 0 & \mathcal{A}_{\mathbf{U}_e\mathbf{V}} & \mathcal{A}_{\mathbf{U}_e} & 0 & \mathcal{A}_{\mathbf{U}_e\mathbf{D}} \\ \mathcal{A}_{\mathbf{\Gamma}_f\mathbf{W}} & 0 & 0 & \mathcal{A}_{\mathbf{\Gamma}_f} & \mathcal{A}_{\mathbf{\Gamma}_f\mathbf{D}} \\ 0 & 0 & 0 & \mathcal{A}_{\mathbf{D}\mathbf{\Gamma}_f} & \mathcal{A}_{\mathbf{D}} \end{pmatrix} \begin{pmatrix} \Delta\mathbf{W}^{(k+1)} \\ \Delta\mathbf{V}^{(k+1)} \\ \Delta\mathbf{U}_e^{(k+1)} \\ \Delta\mathbf{\Gamma}_f^{(k+1)} \\ \Delta\mathbf{D}^{(k+1)} \end{pmatrix} = -\boldsymbol{G}\left(\mathbf{W}^{(k)}, \mathbf{V}^{(k)}, \mathbf{U}_e^{(k)}, \mathbf{\Gamma}_f^{(k)}, \mathbf{D}^{(k)}\right),$$

$$(22)$$

where, given a vector $\boldsymbol{Z}$, we set $\Delta\boldsymbol{Z}^{(k+1)} = \boldsymbol{Z}^{(k+1)} - \boldsymbol{Z}^{(k)}$, and $\boldsymbol{G}(\mathbf{W}, \mathbf{V}, \mathbf{U}_e, \mathbf{\Gamma}_f, \mathbf{D}) = \mathbf{0}$ is the non-linear problem (7) arising at each time step t^{n+1} after discretization. Several remarks are in order:

- The blocks $\mathcal{A}_{\mathbf{WV}}$ and $\mathcal{A}_{\mathbf{VW}}$ come from an implicit treatment of the transmembrane potential and the ionic currents within the ionic model (7c) and the first equation of the bidomain model (7a);

- The blocks $\mathcal{A}_{\mathbf{VD}}$ and $\mathcal{A}_{\mathbf{U}_e\mathbf{D}}$ are due to the dependence of the quantities $\mathbf{F}$ and J in (7a)-(7b) on the solid displacement $\mathbf{d}$ (see Remark 1);

- The blocks $\mathcal{A}_{\mathbf{\Gamma}_f\mathbf{W}}$ and $\mathcal{A}_{\mathbf{\Gamma}_f\mathbf{D}}$ arises from an implicit treatment of the fields w_3 and $\mathbf{d}$ in (7e);

- Finally, the block $\mathcal{A}_{\mathbf{D}\mathbf{\Gamma}_f}$ comes from the dependence of the second Piola-Kirchhoff stress tensor $\mathbf{P}$ on the activation variable γ_f.

Preconditioning for cardiac electromechanical solvers is an active field of research, see [61, 62, 63]. In this work, the block Gauss-Seidel preconditioning

strategy proposed in [64] in the context of FSI problems (FaCSI preconditioning), and then extended in [37] for cardiac electromechanical problems with the monodomain model, is further extended for the Jacobian matrix in (22), with the modifications required by the extra blocks $\mathcal{A}_{\mathbf{VU}_e}$, $\mathcal{A}_{\mathbf{U}_e\mathbf{V}}$ and $\mathcal{A}_{\mathbf{U}_e}$, coming from the bidomain model.

3.3   Space discretization of the electrical problem in the network

For the space discretization of the 1D problem (20) we follow the strategy proposed in [58]. See also [32, 34] for further details. The first three steps in the time marching scheme described above are explicit problems that do not involved any space derivatives (see [58, 32]). Thus, they are solved by simply updating the involved variables nodally. The last step, however, involves a diffusion problem with the following structure,

$$\chi_p \mathcal{C}_p \frac{v_{g,i} - v_{g,i}^\star}{\Delta t} - \left(\frac{L_{i,0}}{L_i(\mathbf{d}^\star)} \right) \frac{\partial}{\partial l} \left(\sigma_p \frac{\partial v_{g,i}}{\partial l} \right) = 0, \quad i = 1, \ldots, P, \qquad (23)$$

where $v_{g,i}^\star$ and $\mathbf{d}^\star$ are known approximations of $v_{g,i}$ and $\mathbf{d}$ at time step t^{n+1}, coming from the previous three steps. The key ingredient in order to enforce the Kirchhoff laws (15a)-(15b) in the global variables v_g and I_g, is to solve (23) using cubic Hermite finite elements. This has the advantage of solving at once the potential variable and its derivative, which is related at each node to the current variable $I_{g,i}$ through (14d). Thus, solving (23) using cubic Hermite finite elements involves degrees of freedom related to the current $I_{g,i}$, and the prescription of (15a)- (15b) can be performed by simply substituting 1's or 0's in the rows related to bifurcation or intersection points of the resulting global discretization matrix associated to the collection of problems (23).

4   Numerical experiments I

4.1   Generalities

In this section, we show the reliability of Algorithm 1 to numerically solve problem (17). The purpose of the presented numerical experiments is twofold. First, we aim at investigating different levels of network-myocardium coupling. In particular, we compare the results obtained with an explicit coupling strategy, i.e., solving the network and the myocardium only once per time step ($K_{max} = 1$ in Algorithm 1), with those obtained with an implicit coupling approach, i.e., iterating between the network and the myocardium subproblems until convergence ($\epsilon = 10^{-7}$ in Algorithm 1). Second, we use Algorithm 1 to investigate the effect of including the Purkinje network in electromechanical simulations in comparison with standard strategies found in the literature to trigger the electrical activation. Special focus is given to mechanical quantities such as ventricle and

(a) Purkinje network and AV node

(b) Fibers field $\mathbf{f}_0$

(c) Sheets field $\mathbf{s}_0$
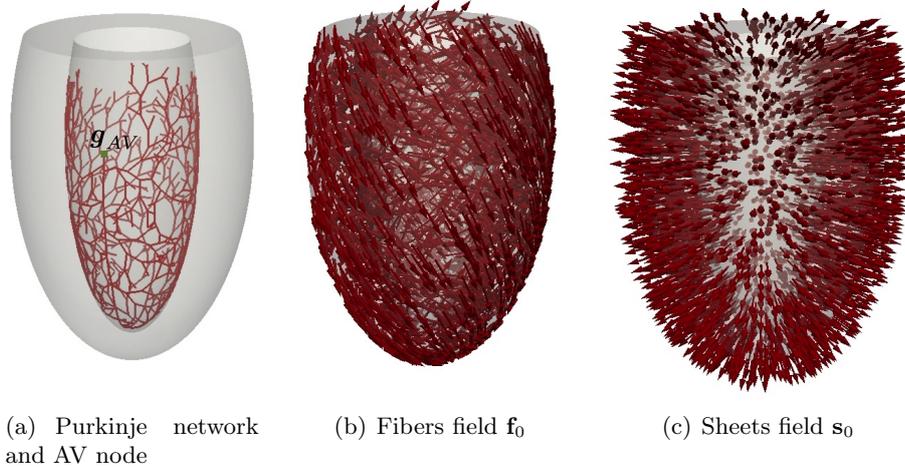
Figure 4: Purkinje network (a), myocardium fibers (b) and sheets (c).

myocardium volumes and nodal displacements. In summary, the numerical tests considered here are:

- *Test I*: Comparisons between implicit and explicit coupling;

- *Test II*: Comparisons between Purkinje and other activation strategies;

The numerical results presented in this work have been obtained with the Finite Element library *LifeV*, developed at MOX - Politecnico di Milano, REO/ESTIME - INRIA, CMCS - EPFL in Lausanne, and E(CM)^2 - Emory University. In particular, the electromechanics and Purkinje network solvers have been developed at MOX - Politecnico di Milano and CMCS - École Polytechnique Fédérale de Lausanne. The discretization in space of the electromechanical problem (7) is carried out using $\mathbb{P}_1$ Lagrangian finite elements for all subproblems (7a)-(7e). The discretization in space of the electrical problem in the network (14) is performed via cubic Hermite finite elements. The time step for solving both problems is $\Delta t = 0.05$ ms. Regarding the ionic models, we use the Bueno-Orovio minimal model [46] for the myocardial cells, whereas the Di Francesco-Noble model [65] is used for the Purkinje cells.

The physical parameters for the (Bueno-Orovio) bidomain system (7a)-(7c) are $\chi_m = 1$ (dimensionless), $C_m = 1$ (dimensionless), $\sigma_{i,t} = 0.19 \cdot 10^{-3}$ (cm^2 ms^{-1}), $\sigma_{e,t} = 2.4 \cdot 10^{-3}$ (cm^2 ms^{-1}), $\sigma_{i,l} = 1.7 \cdot 10^{-3}$ (cm^2 ms^{-1}) and $\sigma_{e,l} = 6.2 \cdot 10^{-3}$ (cm^2 ms^{-1}). The mechanical parameters for the strain-energy function (3) are $B = 5.0 \cdot 10^{-1}$ (g cm^{-1} ms^{-2}), $a = 59 \cdot 10^{-5}$ (g cm^{-1} ms^{-2}), $b = 8.023$ (dimensionless), $a_f = 18472 \cdot 10^{-5}$ (g cm^{-1} ms^{-2}), $b_f = 16.026$ (dimensionless), $a_s = 2481 \cdot 10^{-5}$ (g cm^{-1} ms^{-2}), $b_s = 11.120$ (dimensionless), $a_{fs} = 216 \cdot 10^{-5}$ (g cm^{-1} ms^{-2}) and $b_{fs} = 11.436$ (dimensionless). The myocardium density in (7d) is set to $\rho = 1$ (g cm^{-3}). The constants in (6) are $\lambda_{endo} = 0.5$ (cm),

$\lambda_{epi} = 0.8$ (cm), $k_{endo} = -7.0$ (dimensionless) and $k_{epi} = -5.25$ (dimensionless). The boundary parameters in (8c) are chosen as $K_\perp^{endo} = 1.5 \cdot 10^{-2}$ (g cm^{-2} ms^{-2}), $K_\parallel^{endo} = 1.0 \cdot 10^{-9}$ (g cm^{-2} ms^{-2}), $C_\perp^{endo} = 1.0 \cdot 10^{-1}$ (g cm^{-2} ms^{-1}), $C_\parallel^{endo} = 0$ (g cm^{-2} ms^{-1}), $K_\perp^{epi} = 1.0 \cdot 10^{-4}$ (g cm^{-2} ms^{-2}), $K_\parallel^{epi} = 0$ (g cm^{-2} ms^{-2}), $C_\perp^{epi} = 5.0 \cdot 10^{-1}$ (g cm^{-2} ms^{-1}) and $C_\parallel^{epi} = 0$ (g cm^{-2} ms^{-1}). Finally, the activation parameters in (7e) are $\mu_A = 2.1 \cdot 10^3$ (ms μM^{-2}) and $\varepsilon = 0.05$ (cm^2).

For the monodomain problem in the network (14a)- (14d), we have $\chi_p = 1467$ (cm^{-1}), $R_g = 500$ (kOhm), $r = 0.5$ (cm), $\varrho = 0.0017$ (cm), $R_{\text{PMJ}} = 5$ (kOhm) and $\sigma_p = 35.0$ (kOhm^{-1} cm^{-1}).

For the myocardial geometry we consider the ellipsoidal model of an idealized left ventricle proposed in [48], where the lengths of the semi-principal axes of the inner and outer ellipsoid were $a_x = a_y = 1.5\,\mathrm{cm}\,, a_z = 4.4\,\mathrm{cm}$ and $b_x = b_y = 2.7\,\mathrm{cm}\,, b_z = 5\,\mathrm{cm}$, respectively. See Figure 4. The endocardium surface lays between the planes $z = -4.4$ and $z = 2.2$, whereas the epicardium surface extends form $z = -5$ to $z = 2.2$. For the definition of the vectorial fields $\mathbf{f}_0$ (fibers) and $\mathbf{s}_0$ (sheets), we use the fibers/sheets generation algorithm proposed in [66] and later developed in [67]. The fields obtained are shown in Figures 4 (b) and 4 (c). To generate the mesh, we used the software GMSH [68]. The resulting mesh was composed of about $3.7 \cdot 10^5$ tetrahedra, with $h_m = 0.1$ cm.

The Purkinje network used in this work was the one proposed in [32], which was generated using the method described in [31], consisting in 959 segments and 379 PMJ. See Figure 4 (a). The network covers the endocardial surface between planes $z = -4.4$ and $z = 1.3$. The one-dimensional mesh for the network was composed of 1400 line segments, with $h_p = 0.0165$ cm.

Finally, throughout this section, in which we focus on the effect of the electrophysiology in the mechanics, we will consider $p_{endo}(t) \equiv 0$ in (8d). Thus, the mechanical contraction is exclusively triggered by the electrical activation.

4.2 Test I: Comparisons between implicit and explicit coupling

In this section we study the reduction of the computational cost by considering a weak coupling between the network and the myocardium subproblems. The results are then compared with the ones obtained by strongly coupling network and myocardium. More precisely, we consider the following two solution strategies:

- *Implicit coupling*: Algorithm 1 with $\epsilon = 10^{-7}$ and $K_{max} = 5000$;

- *Explicit coupling*: Algorithm 1 with $K_{max} = 1$;

The experimental setting for Test I goes as follows. Initially the myocardium and network systems are at resting conditions. At $t = 0$, the electric signal is started at the AV node in the network, see Figure 4 (a). The signal travels

through the network and enters the myocardium at the PMJ. The signal then spreads throughout the myocardium triggering the mechanisms leading to the mechanical contraction.

Figure 5, top, shows the evolution of the ventricle and myocardium volumes obtained with the explicit and the implicit coupling strategies during 100 ms. Very good agreement is observed between both strategies. As a matter of fact, the results are indistinguishable from one another. A zoomed window is presented in Figure 5, bottom, showing an error of less than 0.005% in both volumes.

(a) Ventricle volume

(b) Myocardium volume

(c) Ventricle volume

(d) Myocardium volume
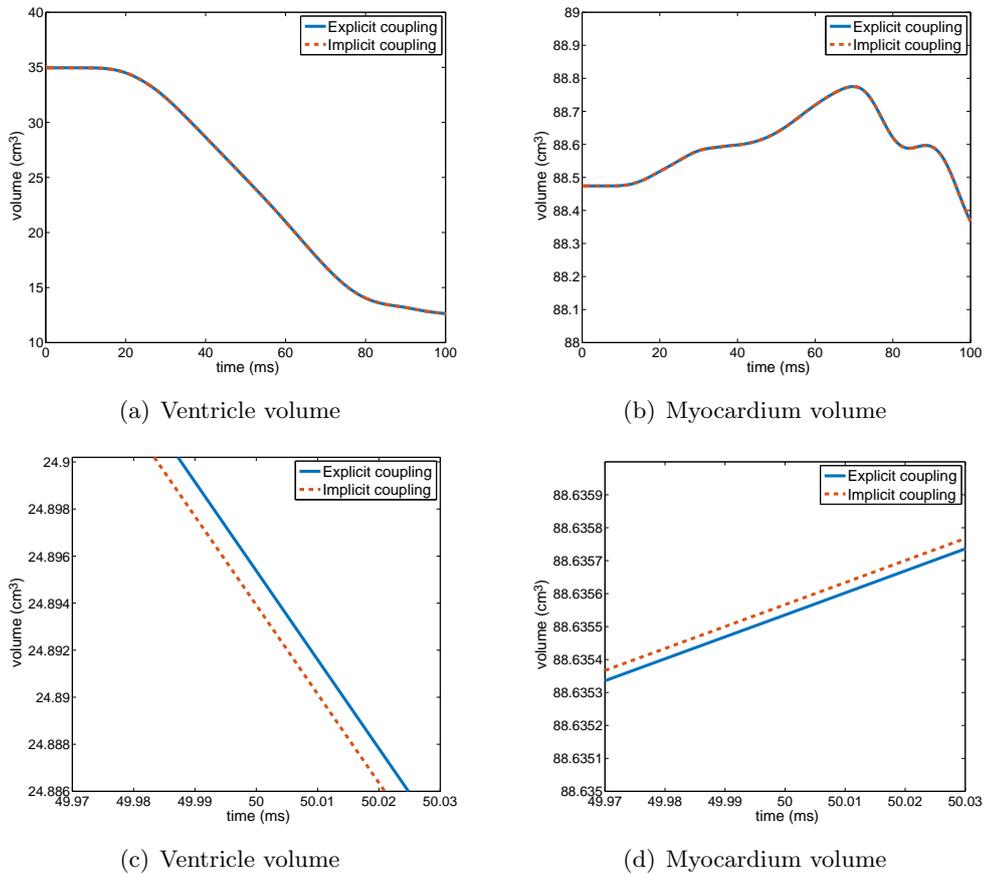
Figure 5: Top: Comparison of ventricle and myocardium volume evolution obtained with the explicit and the implicit coupling strategies. Bottom: Detailed vision of the ventricle and myocardium volume evolution. Test I.

In Figure 6, right, we plot the displacement magnitude at several points of the endocardium and epicardium (see Figure 6, left). Once again, a perfect match of these quantities can be appreciated between the explicit and implicit coupling strategies.
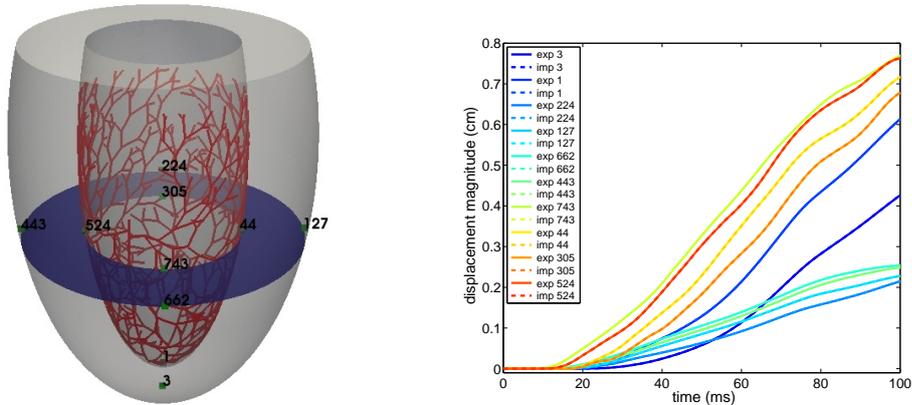
Figure 6: Left: Selected points at the myocardium. Right: Comparison of displacement magnitude $\|\mathbf{d}\|$ at different points with the explicit (exp) and the implicit (imp) coupling strategies. Test I.

From Figures 5 and 6, we conclude that the explicit coupling strategy is an effective way to solve problem (17) without compromising stability and accuracy. As a matter of fact, the simulation involving the implicit coupling required in average 9 iterations per time step between the network and the myocardium subproblems to satisfy a tolerance of $\epsilon = 10^{-7}$. Thus, the explicit scheme is around 9 times faster than the implicit one. In view of these results, for the rest of this paper, we will use the explicit approach to couple the Purkinje network with the myocardium electromechanics.

4.3 Test II: Comparisons between Purkinje network and other activation strategies

In this section we consider standard activation strategies found in the literature and compare them with the results obtained by including the Purkinje network as the source of activation. We will thus compare the solution of the coupled problem (17) with the one of problem (9), in which the external current I^{ext} is properly defined.

A common way to start the depolarization wave in electromechanical simulations is to consider an external initial stimulus at certain points of the myocardium. The stimulus may be triggered simultaneously at all points or with a prescribed delay between them. In [69, 9], for instance, an initial stimulus is applied simultaneously at some nodes located at the upper part of the septum, whereas in [7] the activation is started at the bottom part of the apex. In [70], an external stimulus is applied at different points and time instants in order to initiate a 3-D scroll wave.

For comparison purposes, in this work we consider a time-dependent three-point external stimulus designed according to the synthetic data obtained in
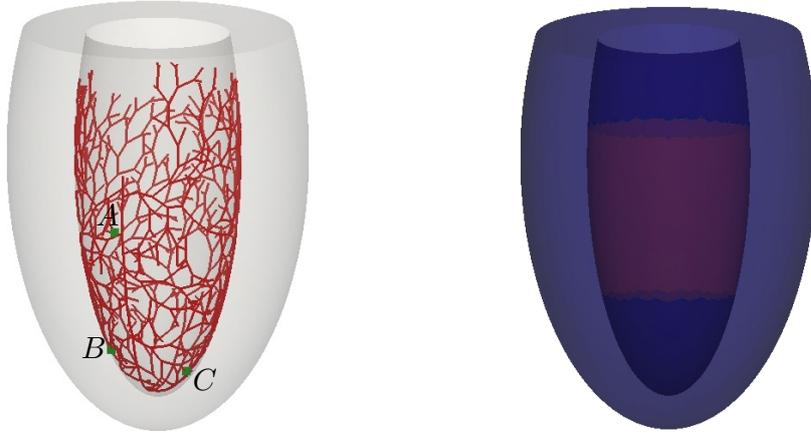
Figure 7: Points (A, B, C) for the 3-points activation (left). Endocardial region for the surface activation (in purple, right).

Section 4.2. To this aim, we selected three points along the network, indicated by A, B and C in Figure 7, left, activated according to the results of Test I. In particular, A is the first PMJ activated (at 5.8 ms), whereas B and C are located downstream (activated at 12.8 ms and 19.4 ms, respectively). Notice that the last PMJ (located at the basal region) was activated at 27.16 ms. The stimuli at these three points last for 2 ms.

Another way to initialize the electric activation is to consider a volume current acting on a thin region of the endocardium surface. This may involve the whole endocardial region [70] or only a central region [11, 67]. In any case, the points of the selected region are activated simultaneously. In this work, we consider the second approach by considering an initial volume current acting for 2 ms on an endocardial region located between the planes $z = 0.5$ and $z = -2.5$, Figure 7, right. It is worth mentioning, that a more sophisticated surface activation strategy accounting for the dynamics of the activation has been used, for instance, in [6], where a space and time dependent volume current is designed, with a propagation speed that has to be properly tuned.

In summary, we consider in this section the following three activation strategies:

- *Purkinje activation*: Coupled problem (17);

- *3-points activation*: Problem (9) with a time-dependent three-point supported I^{ext} (see Figure 7, left);

- *Surface activation*: Problem (9) with a surface supported I^{ext} on the endocardium (see Figure 7, right).

In Figure 8, left, we display the evolution of the ventricle volume (the cavity) obtained with the Purkinje, 3-points, and surface activation strategies. We

see that the three strategies give curves with similar shapes but a discrepancy is observed in the velocity of contraction: the surface activation yields a faster contraction than the Purkinje one, whereas the 3-points activation yields a slightly slower one. This produces a relative difference of about 7% for the 3-points strategy and of about 14% for the surface activation. These discrepancies are also

(a) Ventricle volume   (b) Myocardium volume
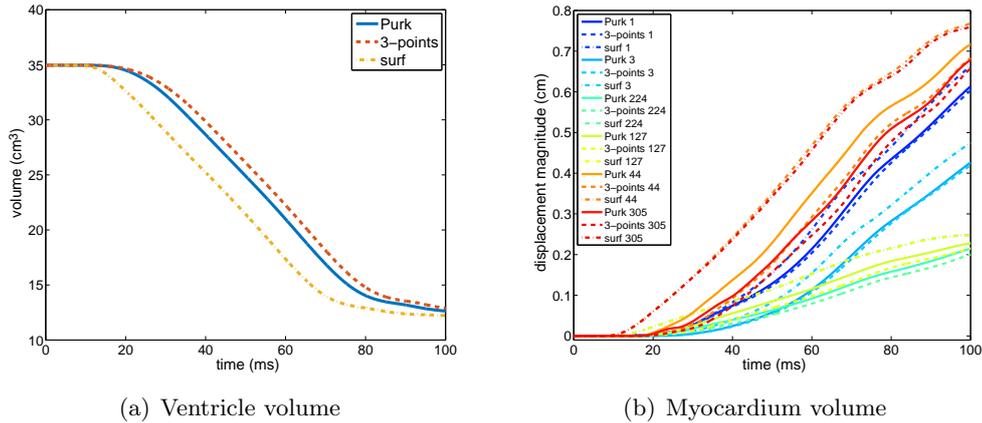
Figure 8: Comparison of the evolution of ventricle volume (left) and ond of displacement magnitude $\|\mathbf{d}\|$ at selected points (right) obtained by Purkinje, 3-points and surface activation. Test II.

highlighted in Figure 8, right, where we compare the displacement magnitude at selected points among those reported in Figure 6, left. We observe again a better approximation with the 3-points activation strategy, in particular in points located close to the apex. However, for points far from the apex, the accuracy of the 3-points activation strategy seems to deteriorate, being comparable with that of the surface activation.

According to these results, we conclude that the mechanical behavior is dependent on the activation strategy adopted. In particular, the surface activation strategy seems to be the less accurate in terms of similarity with the Purkinje network activation strategy. Instead, the 3-points activation strategy is more accurate (again in terms of similarity with the Purkinje network activation strategy). Of course, this strategy could be applied only when activation measurements are available.

5 The Purkinje activation within the Pressure-Volume loop

5.1 A brief introduction to physiology

In view of performing realistic numerical simulations, in this section we provide an overview of the interaction between electrical and mechanical propagations

in the presence of the Purkinje network. In particular, we aim at highlighting the role of the Purkinje network within the Pressure-Volume (PV) loop.
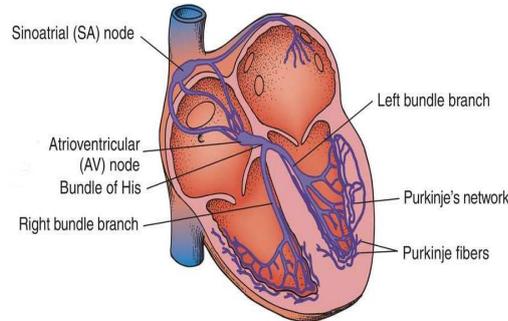
Figure 9: Anatomy of the cardiac conduction system (http://medical-dictionary.thefreedictionary.com)

The electrical activation of the heart is initiated at the sinoatrial (SA) node, which is located in the right atria, near the orifice of the superior vena cava, see Figure 9. The SA node acts as the natural pacemaker of the heart, spontaneously initializing the electrical signal that triggers the Purkinje network and the myocardium activation.

The impulse travels through the atria, via specialized internodal pathways and the atrial myocardial contractile cells themselves, and, after approximately 50 milliseconds (ms), it reaches the AV node, located at the cardiac septum, see Figure 9. The AV node is the unique electrical connection between atria and ventricles, since the connective tissue of the cardiac skeleton acts as an isolator elsewhere. During this lapse of time, the contraction of the atria has already started. The contraction begins in the superior parts and travels downwards, in such a way that the blood is efficiently pumped into the ventricles. Atrial depolarization is associated with the P wave in the electrocardiogram (see, for instance, [71, 10]).

At the AV node, the signal encounters a critical delay of about 75-100 ms. From the mechanical point of view, this delay is extremely important as it allows for the atria to conclude their contraction and pump the blood into the ventricles, before the activation of the ventricles themselves starts. From the AV node, the signal continues to travel through the bundle of His, which is located in the interventricular (IV) septum, and then it splits into the left and right bundle branches. After that, the signal further ramifies and enters the Purkinje network, see Figure 9. The passage from the AV node to the whole Purkinje network takes approximately 25 ms (see, for instance, [71, 72]).

The activation in the left ventricle myocardium starts at the endocardium, where the many activation sites, located at the PMJ, create a propagation wave-front traveling towards the outer wall. The IV septum and the apex are activated 25 ms after the activation of the Purkinje network, and this event corresponds

to the R wave in the electrocardiogram (see, for instance, [71, 10]). The peak of the R wave is associated with the beginning of the isovolumetric contraction of the ventricle (see, for instance, [72]).

During the isovolumetric contraction, the mitral and aortic valves are closed and the intraventricular volume remains unchanged (i.e., there is no ejection). This phase is characterized by the increasing of the pressure inside the ventricle, from the value registered at the end of the diastole (End Diastolic Pressure) to the one within the aorta. When the latter is exceed, the aortic valve opens and the ejection begins. The electrical signal continues to travel during the isovolumetric contraction from the apex to the base and from the endocardium to the epicardium. The S wave in the electrocardiogram corresponds to the activation of the ventricular free walls and the basal region (see, for instance, [10])

Starting from the AV node, the electrical impulse reaches all of the left ventricular muscle cells in about 100 ms. Approximately after that time, the isovolumetric contraction ends and the ejection phase follows, which involves a decrease in the ventricular volume. When the pressure inside the ventricle falls sufficiently, the aortic valve abruptly closes and the isovolumetric relaxation begins, followed by a drastic decrease in the pressure. Finally, the mitral valve opens and the filling phase starts, involving a volume growth in the ventricle until the latter reaches the initial value.

A table showing the relevant correlations between electrical and mechanical events is depicted in Figure 10.

5.2 Efficient detachment of Purkinje network during cardiac cycle simulations

According to these observations, we introduce in what follows an inexact version of Algorithm 1 which is effective for the PV loop computation. Indeed, as observed, the Purkinje network ends its activation after about 25 ms (see Figure 10), whereas the myocardium about 75 ms after the whole network depolarization. Thus, we could think to interrupt the network simulation, and thus the coupling process, after a time $\widetilde{T}$ large enough so that the influence of the Purkinje network could be considered negligible. Accounting for the PMJ delay (about 5 ms) and for the inertia needed by the system to start the front entering in the myocardium, we propose here to set $\widetilde{T} = 80$ ms.

Details on this strategy are presented in Algorithm 2 below. Of course, this algorithm is in principle inexact, being an approximation of Algorithm 1. However, we believe that this could be an effective solution when the whole PV loop is considered, allowing for an accurate solution with reduced computational times.

Location in the heart		Event	Time (ms)	ECG	Mechanics
SA node		impulse generated	0		
atria	right	end depolarization	5	P	start of atrial contraction
	left	end depolarization	85	P	
AV node		arrival of impulse	50		
		departure of impulse	125		full atrial contraction
Purkinje fibers		activation	125 - 150		
endocardium	septum	end depolarization	175	peak of the R wave	start of isovolumetric contraction
	left ventricle	end depolarization	190		
epicardium	left ventricle	end depolarization	225	S	end of isovolumetric contraction

Figure 10: Schematic representation of the relevant correlations between electrical and mechanical events in the left ventricle. Table inspired from [71].

6 Numerical experiments II

In this section, we use Algorithm 2 with $\widetilde{T} = 80$ ms to simulate half heartbeat in the left ventricle. The ventricle and network geometries, as well as the discretization and model parameters, are chosen as in Section 4.1. This simulation is referred in the following as Test III.

6.1 Test III: Pressure-Volume loop with inclusion of the Purkinje network

The simulation begins with the departure of the signal from the AV node, see Figure 4 (a). Thus, time $t = 0$ in the simulation corresponds to time-instant 125 ms in Figure 10. The whole simulation lasts 350 ms and comprises the cardiac systole and the beginning of the filling phase. We consider an initial pressure load, $p_{endo}(0)$ in (8d), equal to 10 mmHg. We follow the pressure prestress strategy described in [37] to compute the initial internal stress distribution in the myocardium such that the reference geometry is in equilibrium with the initial pressure.

In view of the discussion of Section 5, we divide the cardiac cycle in five phases. We consider an initial phase in which the signal travels through the Purkinje network and enters the myocardium. The second phase corresponds to the isovolumetric contraction and it is initialized at $t = 50$ ms (see Figure 10).

The third phase accounts for the blood ejection and it starts when the pressure inside the ventricle reaches a given threshold P^{max}. The fourth phase corresponds to the isovolumetric relaxation and it begins when the ventricle volume starts to increase due to the relaxation of the muscle. Finally, when the pressure inside the ventricle falls down to a given value P^{min}, the fifth phase starts, which corresponds to the filling of the ventricle. To summarize, we split the simulation in the following five phases:

- *Phase 1*: Electric activation phase;

- *Phase 2*: Isovolumetric contraction;

- *Phase 3*: Ejection;

- *Phase 4*: Isovolumetric relaxation;

- *Phase 5*: Filling.

During Phase 1, the endocardial pressure $p_{endo}(t)$ in (8d) is kept equal to 10 mmHg. During Phases 2-4, the dynamics of $p_{endo}(t)$ are dictated by the mechanical interaction of the blood and the endocardium. In order to reproduce such dynamics we use, following [37, 67], zero dimensional models to relate pressure and volume inside the ventricle. During Phases 2 and 4, we enforce a constant ventricle volume to account for the isovolumetric phases using the fixed point strategy proposed in [35, 73], which involves the following pressure-volume elastance models,

$$p_{endo}^{(k+1)} = p_{endo}^{(k)} - \zeta_i(V^{(k)} - V_i^{ref}), \quad i = 2, 4,$$

where the superscript refers to the isovolumetric fixed point iteration, V is the ventricular volume, V_i^{ref}, $i = 2, 4$ the ventricular volume at the beginning of Phases 2 and 4, respectively, and $\zeta_i > 0$, $i = 2, 4$, are penalization parameters. Note that during Phase 2, the volume tends to decrease and thus the pressure increases, whereas in Phase 4, the volume tends to increase and therefore the pressure decreases. For Phase 3, we consider the following two-element Windkessel model (see [73]),

$$C\frac{dp_{endo}}{dt} + \frac{1}{R}p_{endo} = -\frac{dV}{dt},$$

where C and R represents the arterial compliance and resistance.

The additional parameters that have to be fixed for Test III are chosen as $P^{max} = 80.3$ mmHg, $P^{min} = 4.9$ mmHg, $\zeta_2 = 1.5 \cdot 10$ g^{-1} cm ^{4} ms ^{2}, $\zeta_4 = 9.0$ g^{-1} cm ^{4} ms ^{2}, $R = 1.1$ g cm $^{-4}$ ms $^{-1}$ and $C = 1.0 \cdot 10^2$ g^{-1} cm ^{4} ms ^{2}.

In Figure 11 we display the time evolution of the ventricular cavity volume and of the endocardial pressure, and the trajectory in the pressure-volume phase plane. Several comments are in order.

In view of the evolution of the volume and pressure we conclude that Phase 2 corresponds (approximately) to the time interval $[50, 90]$ ms, Phase 3 to $[90, 250]$ ms and Phase 4 to $[250, 310]$ ms. We observe that these values of time intervals perfectly agree with the physiological ones [74, 75].

As expected, the ventricular cavity volume remains approximately constant during Phases 1 and 2, it undergoes a rapid reduction during Phase 3, and during Phase 4 it remains constant at its minimum.

For the endocardium pressure, we found the classical "parabolic" profile during Phase 3, with the rapid upstroke and downstroke during Phases 2 and 4, respectively. The interplay between ventricular cavity volume and endocardial pressure is also shown: we found the classical "rectangular" shape in the pressure-volume phase plane. The overall behavior of the simulation is in good agreement with the expected evolution of physiological pressure-volume trajectories (see [74, 75]).

(a) Ventricle cavity volume   (b) Endocardial pressure   (c) Pressure-Volume trejectory
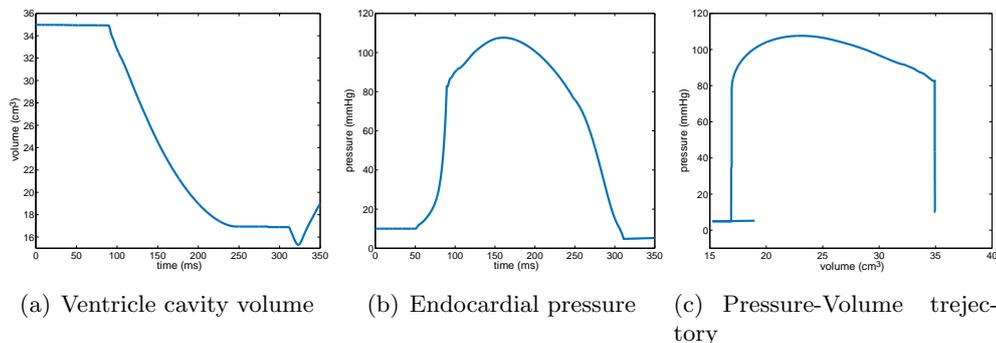
Figure 11: Left: Ventricular cavity volume evolution. Middle: Endocardial pressure evolution. Right: Pressure-Volume trajectory. Test III.

7 Conclusions

A coupling strategy between a 1D electrical model of the Purkinje network and a full 3D electromechanical model of the left ventricle has been proposed. Both these core models represent the state-of-the-art in computational cardiology in their respective domains. The main results found are reviewed in what follows:

1. Implicit and explicit alternatives for the myocardium-network coupling have been investigated. The latter, which provides stable and accurate solutions, has proved to be an efficient and advisable alternative to implicit coupling;

2. A comparison study has shown that the mechanical response of the myocardium obtained by including the electrophysiology of the Purkinje net-

work cannot be completely reproduced by other surrogate standard activation strategies found in the literature;

3. A detailed description of the role of the Purkinje network in a physiological cardiac simulation has been presented and simulated. Physiological results have been obtained, which highlight the suitability of the proposed strategy to include the Purkinje activation in the ventricle electrophysiology.

Further investigations of the present work in view of an application to real geometries, possibly in unhealthy conditions, are currrently under study.

Acknowledgements

References

[1] Hunter P, Nash M, Sands G. Computational electromechanics of the heart. *Computational biology of the heart* 1997; **12**:347–407.

[2] Smith N, Nickerson D, Crampin E, Hunter P. Multiscale computational modelling of the heart. *Acta Numerica* 2004; **13**:371–431.

[3] Kerckhoffs R, Healy S, Usyk T, McCulloch A. Computational methods for cardiac electromechanics. *Proceedings of the IEEE* 2006; **94**(4):769–783.

[4] Boulakia M, Fernández M, Gerbeau J, Zemzemi N. Direct and inverse problems in electrocardiography. *AIP Conference Proceedings*, vol. 1048, AIP, 2008; 113–117.

[5] Niederer S, Smith N. An improved numerical method for strong coupling of excitation and contraction models in the heart. *Progress in biophysics and molecular biology* 2008; **96**(1):90–111.

[6] Boulakia M, Cazeau S, Fernández MA, Gerbeau JF, Zemzemi N. Mathematical modeling of electrocardiograms: a numerical study. *Annals of biomedical engineering* 2010; **38**(3):1071–1097.

[7] Ambrosi D, Arioli G, Nobile F, Quarteroni A. Electromechanical coupling in cardiac dynamics: the active strain approach. *SIAM Journal on Applied Mathematics* 2011; **71**(2):605–621.

[8] Nordsletten D, Niederer S, Nash M, Hunter P, Smith N. Coupling multi-physics models to cardiac mechanics. *Progress in biophysics and molecular biology* 2011; **104**(1):77–88.

[9] Wong J, Göktepe S, Kuhl E. Computational modeling of chemo-electro-mechanical coupling: A novel implicit monolithic finite element approach. *International journal for numerical methods in biomedical engineering* 2013; **29**(10):1104–1133.

[10] Colli Franzone P, Pavarino L, Scacchi S. *Mathematical cardiac electrophysiology*, vol. 13. Springer, 2014.

[11] Rossi S, Lassila T, Ruiz-Baier R, Sequeira A, Quarteroni A. Thermodynamically consistent orthotropic activation model capturing ventricular systolic wall thickening in cardiac electromechanics. *European Journal of Mechanics-A/Solids* 2014; **48**:129–142.

[12] Lee J, Cookson A, Roy I, Kerfoot E, Asner L, Vigueras G, Sochi T, Deparis S, Michler C, Smith N, *et al.*. Multiphysics computational modeling in cheart. *SIAM Journal on Scientific Computing* 2016; **38**(3):C150–C178.

[13] Chabiniok R, Wang V, Hadjicharalambous M, Asner L, Lee J, Sermesant E Mand Kuhl, Young A, Moireau P, Nash MP, *et al.*. Multiphysics and multiscale modelling, data–model fusion and integration of organ physiology in the clinic: ventricular cardiac mechanics. *Interface focus* 2016; **6**(2):20150 083.

[14] Quarteroni A, Lassila T, Rossi S, Ruiz-Baier R. Integrated heart—coupling multiscale and multiphysics models for the simulation of the cardiac function. *Computer Methods in Applied Mechanics and Engineering* 2017; **314**:345–407.

[15] Quarteroni A, Manzoni A, Vergara C. The cardiovascular system: Mathematical modelling, numerical algorithms and clinical applications. *Acta Numerica* 2017; **26**:365–590.

[16] Colli Franzone P, Pavarino LF, Scacchi S. Bioelectrical effects of mechanical feedbacks in a strongly coupled cardiac electro-mechanical model. *Mathematical Models and Methods in Applied Sciences* 2016; **26**(01):27–57.

[17] Colli Franzone P, Pavarino L, Scacchi S. Effects of mechanical feedback on the stability of cardiac scroll waves: A bidomain electro-mechanical simulation study. *Chaos: An Interdisciplinary Journal of Nonlinear Science* 2017; **27**(9):093 905.

[18] Trayanova N, Li W, Eason J, Kohl P. Effect of stretch-activated channels on defibrillation efficacy. *Heart Rhythm* 2004; **1**(1):67–77.

[19] Trayanova N. Defibrillation of the heart: insights into mechanisms from modelling studies. *Experimental physiology* 2006; **91**(2):323–337.

[20] Vigmond E, Stuyvers B. Modeling our understanding of the His-Purkinje system. *Progress in biophysics and molecular biology* 2016; **120**(1):179–188.

[21] Abboud S, Berenfeld O, Sadeh D. Simulation of high-resolution qrs complex using a ventricular model with a fractal conduction system. effects of ischemia on high-frequency qrs potentials. *Circulation Research* 1991; **68**(6):1751–1760.

[22] Behradfar E, Nygren A, Vigmond EJ. The role of Purkinje-myocardial coupling during ventricular arrhythmia: A modeling study. *PLOS ONE* 2014; **9**(2):1–9.

[23] Ijiri i T, Ashihara T, Yamaguchi Y, Takayama K, Igarashi T, Shimada T, Namba T, Haraguchi R, Nakazawa K. A procedural method for modeling the Purkinje fibers of the heart. *The journal of physiological sciences* 2008; **58**(7):481–486.

[24] Deo M, Boyle P, Kim A, Vigmond E. Arrhythmogenesis by single ectopic beats originating in the Purkinje system. *American Journal of Physiology-Heart and Circulatory Physiology* 2010; **299**(4):H1002–H1011.

[25] Pashaei A, Romero D, Sebastian R, Camara O, Frangi A. Fast multi-scale modeling of cardiac electrophysiology including Purkinje system. *IEEE Transactions on Biomedical Engineering* 2011; **58**(10):2956–2960.

[26] Clayton R, Bernus O, Cherry E, Dierckx H, Fenton F, Mirabella L, Panfilov A, Sachse F, Seemann G, Zhang H. Models of cardiac tissue electrophysiology: progress, challenges and open questions. *Progress in biophysics and molecular biology* 2011; **104**(1):22–48.

[27] Sebastian R, Zimmerman V, Romero D, Frangi A. Construction of a computational anatomical model of the peripheral cardiac conduction system. *IEEE Transactions on Biomedical Engineering* 2011; **58**(12):3479–3482.

[28] Vergara C, Palamara S, Catanzariti D, Nobile F, Faggiano E, Pangrazzi C, Centonze M, Maines M, Quarteroni A, Vergara G. Patient-specific generation of the Purkinje network driven by clinical measurements of a normal propagation. *Medical and Biological Engineering and Computing* 2014; **52**(10):813.

[29] Palamara S, Vergara C, Catanzariti D, Faggiano E, Pangrazzi C, Centonze M, Nobile F, Maines M, Quarteroni A. Computational generation of the Purkinje network driven by clinical measurements: the case of pathological propagations. *International journal for numerical methods in biomedical engineering* 2014; **30**(12):1558–1577.

[30] Walton R, Martinez M, Bishop M, Hocini M, Haïssaguerre M, Plank G, Bernus O, Vigmond E. Influence of the Purkinje-muscle junction on transmural repolarization heterogeneity. *Cardiovascular research* 2014; **103**(4):629–640.

[31] Palamara S, Vergara C, Faggiano E, Nobile F. An effective algorithm for the generation of patient-specific Purkinje networks in computational electrocardiology. *Journal of Computational Physics* 2015; **283**:495–517.

[32] Vergara C, Lange M, Palamara S, Lassila T, Frangi A, Quarteroni A. A coupled 3d–1d numerical monodomain solver for cardiac electrical activation in the myocardium with detailed Purkinje network. *Journal of Computational Physics* 2016; **308**:218–238.

[33] Neic A, Campos F, Prassl A, Niederer S, Bishop M, Vigmond E, Plank G. Efficient computation of electrograms and ECGs in human whole heart simulations using a reaction-eikonal model. *Journal of Computational Physics* 2017; **346**:191 – 211.

[34] Lange M, Palamara S, Lassila T, Vergara C, Quarteroni A, Frangi A. Improved hybrid/gpu algorithm for solving cardiac electrophysiology problems on Purkinje networks. *International Journal for Numerical Methods in Biomedical Engineering* 2017; **33**(6):e2835–n/a.

[35] Usyk T, LeGrice I, McCulloch A. Computational model of three-dimensional cardiac electromechanics. *Computing and Visualization in Science* 2002; **4**(4):249–257.

[36] Palamara S. Numerical approximation of the electrical activity in the left ventricle with the inclusion of the Purkinje fibers. PhD Thesis, Politecnico di Milano 2015.

[37] Gerbi A, Dede' L, Quarteroni A. A monolithic algorithm for the simulation of cardiac electromechanics in the human left ventricle. *MOX-Report No. 51/2017* 2017; .

[38] Rossi S, Ruiz-Baier R, Pavarino L, Quarteroni A. Orthotropic active strain models for the numerical simulation of cardiac biomechanics. *International Journal for Numerical Methods in Biomedical Engineering* 2012; **28**(6-7):761–788.

[39] Holzapfel G, Ogden R. Constitutive modelling of passive myocardium: a structurally based framework for material characterization. *Philosophical Transactions of the Royal Society of London A: Mathematical, Physical and Engineering Sciences* 2009; **367**(1902):3445–3475.

[40] Kohl P, Hunter P, Noble D. Stretch-induced changes in heart rate and rhythm: clinical observations, experiments and mathematical models. *Progress in biophysics and molecular biology* 1999; **71**(1):91–138.

[41] Colli Franzone P, Pavarino L, Savaré G. Computational electrocardiology: mathematical and numerical modeling. *Complex systems in biomedicine*. Springer, 2006; 187–241.

[42] Hodgkin A, Huxley A. A quantitative description of membrane current and its application to conduction and excitation in nerve. *The Journal of physiology* 1952; **117**(4):500–544.

[43] Luo C, Rudy Y. A model of the ventricular cardiac action potential. depolarization, repolarization, and their interaction. *Circulation research* 1991; **68**(6):1501–1526.

[44] Iyer V, Mazhari R, Winslow R. A computational model of the human left-ventricular epicardial myocyte. *Biophysical journal* 2004; **87**(3):1507–1525.

[45] Ten Tusscher K, Panfilov A. Modelling of the ventricular conduction system. *Progress in biophysics and molecular biology* 2008; **96**(1):152–170.

[46] Bueno-Orovio A, Cherry E, Fenton FH. Minimal model for human ventricular action potentials in tissue. *Journal of theoretical biology* 2008; **253**(3):544–560.

[47] Keener J, Bogar K. A numerical method for the solution of the bidomain equations in cardiac tissue. *Chaos: An Interdisciplinary Journal of Nonlinear Science* 1998; **8**(1):234–241.

[48] Franzone PC, Guerri L, Pennacchio M, Taccardi B. Spread of excitation in 3-d models of the anisotropic cardiac tissue. ii. effects of fiber architecture and ventricular geometry. *Mathematical biosciences* 1998; **147**(2):131–171.

[49] Vigmond E, Aguel F, Trayanova N. Computational techniques for solving the bidomain equations in three dimensions. *IEEE Transactions on Biomedical Engineering* 2002; **49**(11):1260–1269.

[50] Colli Franzone P, Pavarino L. A parallel solver for reaction-diffusion systems in computational electrocardiology. *Math. Models Methods Appl. Sci.* 2004; **14**(6):883–911.

[51] Tung L. A bi-domain model for describing ischemic myocardial dc potentials. PhD Thesis, Massachusetts Institute of Technology 1978.

[52] Usyk T, Mazhari R, McCulloch A. Effect of laminar orthotropic myofiber architecture on regional stress and strain in the canine left ventricle. *Journal of elasticity and the physical science of solids* 2000; **61**(1-3):143–164.

[53] Costa K, Holmes JW, McCulloch A. Modelling cardiac mechanical properties in three dimensions. *Philosophical Transactions of the Royal Society of London A: Mathematical, Physical and Engineering Sciences* 2001; **359**(1783):1233–1250.

[54] Nobile F, Quarteroni A, Ruiz-Baier R. An active strain electromechanical model for cardiac tissue. *International journal for numerical methods in biomedical engineering* 2012; **28**(1):52–71.

[55] Ambrosi D, Pezzuto S. Active stress vs. active strain in mechanobiology: constitutive issues. *Journal of Elasticity* 2012; **107**(2):199–212.

[56] Gordon A, Huxley A, Julian F. The variation in isometric tension with sarcomere length in vertebrate muscle fibres. *The Journal of physiology* 1966; **184**(1):170–192.

[57] Barbarotta L, Rossi S, Dede' L, Quarteroni A. A transmurally heterogeneous orthotropic activation model for ventricular contraction and its numerical validation. *MOX-Report No. ??/2017* 2017; .

[58] Vigmond E, Clements C. Construction of a computer model to investigate sawtooth effects in the Purkinje system. *IEEE Transactions on Biomedical Engineering* 2007; **54**(3):389–399.

[59] Bordas S, Gillow K, Gavaghan D, Rodríguez B, Kay D. A bidomain model of the ventricular specialized conduction system of the heart. *SIAM Journal on Applied Mathematics* 2012; **72**(5):1618–1643.

[60] Pathmanathan R, Mirams G, Southern J, Whiteley J. The significant effect of the choice of ionic current integration method in cardiac electrophysiological simulations. *International Journal for Numerical Methods in Biomedical Engineering* 2011; **27**(11):1751–1770.

[61] Franzone PC, Pavarino LF, Scacchi S. Parallel multilevel solvers for the cardiac electro-mechanical coupling. *Applied Numerical Mathematics* 2015; **95**:140–153.

[62] Pavarino L, Scacchi S, Zampini S. Newton–krylov-bddc solvers for nonlinear cardiac mechanics. *Computer Methods in Applied Mechanics and Engineering* 2015; **295**:562–580.

[63] Franzone PC, Pavarino L, Scacchi S. Joint influence of transmural heterogeneities and wall deformation on cardiac bioelectrical activity: a simulation study. *Mathematical biosciences* 2016; **280**:71–86.

[64] Deparis S, Forti D, Grandperrin G, Quarteroni A. Facsi: A block parallel preconditioner for fluid–structure interaction in hemodynamics. *Journal of Computational Physics* 2016; **327**:700–718.

[65] DiFrancesco D, Noble D. A model of cardiac electrical activity incorporating ionic pumps and concentration changes. *Philosophical Transactions of the Royal Society of London B: Biological Sciences* 1985; **307**(1133):353–398.

[66] Wong J, Kuhl E. Generating fibre orientation maps in human heart models using poisson interpolation. *Computer methods in biomechanics and biomedical engineering* 2014; **17**(11):1217–1226.

[67] Rossi S. Anisotropic modeling of cardiac mechanical activation. PhD Thesis, EPFL 2014.

[68] Geuzaine C, Remacle JF. Gmsh: A 3-d finite element mesh generator with built-in pre-and post-processing facilities. *International journal for numerical methods in engineering* 2009; **79**(11):1309–1331.

[69] Göktepe S, Kuhl E. Electromechanics of the heart: a unified approach to the strongly coupled excitation–contraction problem. *Computational Mechanics* 2010; **45**(2):227–243.

[70] Keldermann RH, Nash MP, Gelderblom H, Wang VY, Panfilov AV. Electromechanical wavebreak in a model of the human left ventricle. *American Journal of Physiology-Heart and Circulatory Physiology* 2010; **299**(1):H134–H143.

[71] Malmivuo J, Plonsey R. *Bioelectromagnetism: principles and applications of bioelectric and biomagnetic fields*. Oxford University Press, USA, 1995.

[72] CNX O. Openstax, anatomy and physiology, http://cnx.org/contents/14fb4ad7-39a1-4eee-ab6e-3ef2482e3e22@8.108.

[73] Eriksson TS, Prassl A, Plank G, Holzapfel GA. Influence of myocardial fiber/sheet orientations on left ventricular mechanical contraction. *Mathematics and Mechanics of Solids* 2013; **18**(6):592–606.

[74] Greene M, Jun JC, Mohr D, Bourland H. A mathematical model of left-ventricular function. *Medical and biological engineering* 1973; **11**(2):126–134.

[75] Keener J, Sneyd J. *Mathematical physiology: II: Systems Physiology*. Springer Science & Business Media, 2009.

Algorithm 1 *Solution of the discretized-in-time Myocardium-Network coupled problem*

Let k be the iteration index within each time step. Set $k = 0$ and

$$\varphi_j^{(0)} = \varphi_{0,j} := \frac{\frac{\left(v_p^+\right)^n(\boldsymbol{g}_j)+\left(v_p^-\right)^n(\boldsymbol{g}_j)}{2} - \frac{1}{A_r}\int_{\mathcal{B}_r(\boldsymbol{g}_j)} v_m^n\, d\boldsymbol{x}}{R_{PMJ}}, \quad j = 1,\ldots,N, \quad (18)$$

with $\left(v_p^+\right)^n$, $\left(v_p^-\right)^n$, v_m^n the converged solution at the previous time step, and choose a tolerance $\epsilon > 0$;

while $\left(\|\boldsymbol{\varphi}^{(k)} - \boldsymbol{\varphi}^{(k-1)}\| > \epsilon \text{ and } k < K_{max}\right)$

1. Solve the discretized-in-time electromechanics problem (7) in the myocardium with applied currents given by $\boldsymbol{\varphi}^{(k)}$, that is

$$\boldsymbol{P}_m\left(v_m^{(k+1)}, u_{e,m}^{(k+1)}, \mathbf{w}_m^{(k+1)}, \mathbf{d}^{(k+1)}, \gamma_f^{(k+1)}, \sum_{j=1}^N \frac{1}{A_r}\mathcal{I}_{\mathcal{B}_r(\boldsymbol{s}_j)}\varphi_j^{(k)}\right) = \mathbf{0}; \quad (19)$$

2. Solve the discretized-in-time monodomain problem (10) in the Purkinje network with Neumann boundary conditions at the PMJ given by $\boldsymbol{\varphi}^{(k)}$, that is

$$\boldsymbol{P}_p\left((v_p^+)^{(k+1)}, (v_p^-)^{(k+1)}, v_g^{(k+1)}, I_g^{(k+1)}, (\mathbf{w}_p^+)^{(k+1)}, (\mathbf{w}_p^-)^{(k+1)}, \mathbf{d}^{(k+1)}, \boldsymbol{\varphi}^{(k)}\right) = \mathbf{0};$$
$$(20)$$

3. Compute

$$\varphi_j^{(k+1)} = \frac{\frac{\left(v_p^+\right)^{(k+1)}(\boldsymbol{g}_j)+\left(v_p^-\right)^{(k+1)}(\boldsymbol{g}_j)}{2} - \frac{1}{A_r}\int_{\mathcal{B}_r(\boldsymbol{g}_j)} v_m^{(k+1)}\, d\boldsymbol{x}}{R_{PMJ}}, \quad j = 1,\ldots,N;$$
$$(21)$$

4. Set $k = k + 1$.

end

Algorithm 2 *Efficient solution of the discretized-in-time Myocardium-Network coupled problem*

Given $\widetilde{T}$,

if $t \leq \widetilde{T}$ **then**

set k be the iteration index within each time step. Set $k = 0$, $\varphi_j^{(0)}$ given by (18) and choose a tolerance $\varepsilon > 0$;

   while $\left(\|\boldsymbol{\varphi}^{(k)} - \boldsymbol{\varphi}^{(k-1)}\| > \varepsilon \text{ and } k < K_{max} \right)$

   1. Solve the discretized-in-time electromechanics problem (7) in the myocardium with applied currents given by $\boldsymbol{\varphi}^{(k)}$, that is

$$
\boldsymbol{P}_m \left(v_m^{(k+1)}, u_{e,m}^{(k+1)}, \mathbf{w}_m^{(k+1)}, \mathbf{d}^{(k+1)}, \gamma_f^{(k+1)}, \sum_{j=1}^{N} \frac{1}{A_r} \mathcal{I}_{\mathcal{B}_r(\boldsymbol{s}_j)} \varphi_j^{(k)} \right) = \mathbf{0};
$$

   2. Solve the discretized-in-time monodomain problem (10) in the Purkinje network with Neumann boundary conditions at the PMJ given by $\boldsymbol{\varphi}^{(k)}$, that is

$$
\boldsymbol{P}_p \left((v_p^+)^{(k+1)}, (v_p^-)^{(k+1)}, v_g^{(k+1)}, I_g^{(k+1)}, (\mathbf{w}_p^+)^{(k+1)}, (\mathbf{w}_p^-)^{(k+1)}, \mathbf{d}^{(k+1)}, \boldsymbol{\varphi}^{(k)} \right) = \mathbf{0};
$$

   3. Compute

$$
\varphi_j^{(k+1)} = \frac{\frac{(v_p^+)^{(k+1)}(\boldsymbol{g}_j) + (v_p^-)^{(k+1)}(\boldsymbol{g}_j)}{2} - \frac{1}{A_r} \int_{\mathcal{B}_r(\boldsymbol{g}_j)} v_m^{(k+1)} \, d\boldsymbol{x}}{R_{PMJ}}, \quad j = 1, \dots, N;
$$

   4. Set $k = k + 1$.

   end while

else

   Solve the discretized-in-time electromechanics problem (7) in the myocardium with applied currents given by $\boldsymbol{\varphi} = \mathbf{0}$, that is

$$
\boldsymbol{P}_m \left(v_m, u_{e,m}, \mathbf{w}_m, \mathbf{d}, \gamma_f, 0 \right) = \mathbf{0}.
$$

end if

MOX Technical Reports, last issues

Dipartimento di Matematica
Politecnico di Milano, Via Bonardi 9 - 20133 Milano (Italy)

56/2017   Alberti, G. S.; Santacesaria, M.
Infinite dimensional compressed sensing from anisotropic measurements

57/2017   Ballarin, F.; D'Amario, A.; Perotto, S.; Rozza, G.
A POD-Selective Inverse Distance Weighting method for fast parametrized shape morphing

55/2017   Agosti, A.; Cattaneo, C.; Giverso, C.; Ambrosi, D.; Ciarletta, P.
A computational platform for the personalized clinical treatment of glioblastoma multiforme

54/2017   Dede', L; Quarteroni, A.
Isogeometric Analysis of a Phase Field Model for Darcy Flows with Discontinuous Data

53/2017   Bertagna, L.; Deparis, S.;Formaggia, L.; Forti, D.; Veneziani A.
The LifeV library: engineering mathematics beyond the proof of concept

52/2017   Beretta, E.; Ratti, L.; Verani, M.
A phase-field approach for the interface reconstruction in a nonlinear elliptic problem arising from cardiac electrophysiology

51/2017   Gerbi, A.; Dede', L.; Quarteroni, A.
A monolithic algorithm for the simulation of cardiac electromechanics in the human left ventricle

50/2017   Formaggia, F.; Vergara, C.
Defective boundary conditions for PDEs with applications in haemodynamics

49/2017   Antonietti, P. F.,; Pennesi, G.
V-cycle multigrid algorithms for discontinuous Galerkin methods on non-nested polytopic meshes

48/2017   Regazzoni, F.; Dedè, L.; Quarteroni, A.
Active contraction of cardiac cells: a model for sarcomere dynamics with cooperative interactions